SAND2021-7200C

Modeling Grid-Forming Inverter Dynamics Under Ground Fault Scenarios Using Experimental Data From Commercially Available Equipment

Javier Hernández-Alvídrez, Nicholas S. Gurule, Rachid Darbali-Zamora,
Matthew J. Reno, and Jack D. Flicker

Sandia National Laboratories, Albuquerque, New Mexico, 87123, United States.

Abstract— **In order to address the recent inclement weather-related energy events, electricity production is experiencing an important transition from conventional fossil fuel based resources to the use of Distributed Energy Resources (DER), providing clean and renewable energy. These DERs make use of power electronic based devices that perform the energy conversion process required to interface with the utility grids. For the particular cases where DC/AC conversion is required, grid-forming inverters (GFMI) are gaining popularity over their grid-following (GFLI) counterpart. This is due to the fact that GFMI do not require a dedicated Phase Locked Loop (PLL) to synchronize with the grid. The absence of a PLL allows GFMI to operate in stand-alone (off-grid) mode when needed. Nowadays, inverter manufacturers are already offering several products with grid-forming capabilities. However, modeling the dynamics of commercially available GFMI under heavy loads or faults scenarios has become a critical task not only for stability studies, but also for coordination and protection schemes in power grids (or microgrids) that are experiencing a steady growth in their levels of DERs. Based upon experimental low-impedance fault results performed on a commercially available GFMI, this paper presents a modeling effort to replicate the dynamics of such inverters under these abnormal scenarios. The proposed modeling approach relies on modifying previously developed GFMI models, by adding the proper dynamics, to match the current and voltage transient behavior under low-impedance fault scenarios. For the first inverter tested, a modified CERTS GFMI model provides matching transient dynamics under faults scenarios with respect to the experimental results from the commercially available inverter.**

keywords—renewable energy, grid-forming, inverter, faults, converter modeling, experimental results.

I. INTRODUCTION

From the energy generation and transmission perspective, addressing the legitimate concerns in regard to the environmental footprints caused by the massive use of fossil fuels has become a critical initiative among utility companies and governmental energy agencies around the world [1]-[2]. While the energy generation paradigm is shifting away from conventional fossil fueled resources to a systemic and gradual increase in the use of sustainable renewable resources, the state of practice must also transition from reactive to resilient [3]. In such a scenario, renewable Distributed Energy Resources (DERs) should not only be able to provide for the energy demands, but also coordinate with the main generation sources in the grid and the end customers in order to maintain the system's stability, reliability, and protection. Emerging microgrid architectures demand the use of novel and adaptable power electronic interfaces that have the ability to manage DER regardless of the presence of a conventional energy source providing the main power to the microgrid [4]-[5]. The flexibility of a well-managed DER allows them to transition from grid-tied to islanded scenarios, combined with the ability to share the load demands with other DER, provide significant benefits in contingency scenarios that challenge the integrity of the system in the form of natural disasters or extreme weather conditions [6]. The key technical route to achieve this type of dynamics is by using cooperative synchronization [7], which not only allows for a stable dynamical compatibility between DER, but also permits them to transition and operate from a hierarchical power management to a more lateral and democratized perspective [8]-[9].

The proliferation of the interconnection of grid-following inverters (GFLIs) into hybrid power systems, along with the proper use of the ancillary functions that they provide [10]-[11] (e.g. volt-var, frequency-watt, fixed power factor) make GFLIs extremely useful to improve resiliency and stability by means of voltage [12] and frequency regulation. However, one of the main drawbacks of GFLI is the requirement of a synchronization mechanism, such as a phase locked loop (PLL), which allows the required phase-angle tracking with the grid [13]. In the absence of a stiff voltage reference at their point of common coupling (PCC), GFLI cease to operate, causing a significant drop in the power provided by them. This poses the risk of completely losing power services in cases where only GFLI are used as DER. In order to comply with the autonomous synchronization demands imposed on their DER constituents by modern microgrid control architectures, grid-forming inverters (GFMI) respond to this call due to their intrinsic synchronization control scheme embedded in the droop regulation characteristics in their frequency and voltage controllers [9],[14]. GFMI have the ability to control voltage and frequency at their PCC, similar to that of a synchronous generator (SG). This means that they can help in supporting the system's frequency and voltage while also providing power to the system loads, decreasing the dependency of mechanical inertia from SGs. Previous research has demonstrated that the benefits of using GFMI to replace diesel generators in microgrids to provide spinning reserve

Sandia National Laboratories is a multimission laboratory managed and operated by National Technology & Engineering Solutions of Sandia, LLC, a wholly owned subsidiary of Honeywell International Inc., for the U.S. Department of Energy's National Nuclear Security Administration under contract DE-NA0003525.

devices by improving the frequency nadir during partial power loss scenarios [15].

Currently, the modeling and integration of new GFMI control schemes is a very active line of research. The model provided by The Consortium for Electric Reliability Technology Solutions (CERTS) [16] has been widely used due to its simple and highly reliable control scheme, allowing both voltage and frequency regulation. Furthermore, the CERTS model presents an upgraded version in [17], which addresses the problem of GFMI dynamics during overloading conditions, a topic normally overseen but of great importance. Another widely used GFMI model is the virtual synchronous generator (VSG) [18], also referred to as synchronverter in [8]-[9]. The VSG emulates the dynamic equations of a SG embedded in its control scheme. This scheme utilizes the concepts of emulated inertia time-constant and virtual impedance, which are programmable input parameters allocated in the memory of the VSG controller, as in the case of the commercially available ABB PCS-100 inverter [19]. Lastly, another highly promising GFMI model is the virtually controlled oscillator (VCO) scheme [20]–[23] which explores the inherent synchronization dynamics of non-linear oscillators to provide grid-forming capabilities.

The inherent nature of GFMI is to follow the supplied loads, making them prone to severe overcurrent transients in the presence of low-impedance faults. Therefore, accurate modeling of these dynamics, particularly of the GFMI available in the market, is crucial to understand and analyze. Furthermore, inverter manufacturers are reluctant to provide useful information to aid in the modeling due to intellectual property conflicts. Herein, this paper complements the work reported in [24]-[25] by providing GFMI models that replicate the dynamics of the experimental results of such inverters under ground fault scenarios. The presented experimental results for grounded faults were performed in the Distributed Energy Technologies Laboratory (DETL) located at Sandia National Laboratories.

II. Model with Voltage and Current Clipping

A. Theoretical Background

Based on voltage and current traces reported in [24]-[25], it can be observed that their magnitudes are clipped right after a fault occurrence. This protection scheme resembles the constant current curtailment method widely used in DC/DC converters [26], where voltage-current characteristics are shown in Fig. 1.

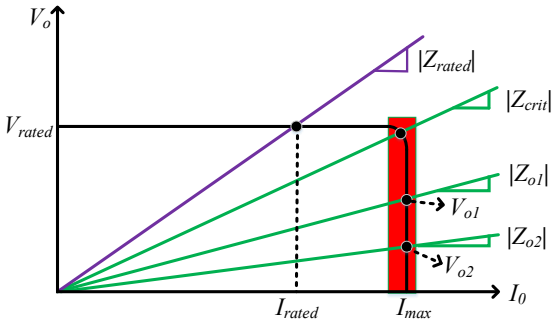

Fig. 1. Voltage-Current Characteristics of Constant Current Protection Mode for DC/DC Converters.

The green traces represent different linear load characteristics that drive the converter under overloading or fault conditions. When the converter operates within rated current values, the voltage is regulated regardless of the current being supplied to the load, which is represented by the purple line labeled $|Z_{rated}|$. As the load impedance decreases and approaches to $|Z_{crit}|$, a critical point is reached where the maximum permissible current, I_{max} is being supplied. At this point, the constant-current curtailment scheme is enabled, as shown by the red area in Fig. 1. Notice that as the load impedance decreases below $|Z_{crit}|$ the magnitude of the supplied voltage also decreases while curtailing the output current to I_{max}. In the case of a GFMI, the output current is determined by the maximum allowable current of the semiconductor switches that form the H-Bridge where the DC/AC power conversion takes place. That is to say, this current protection scheme is used to protect the semiconductor devices of a power converter against severe overcurrent scenarios by modulating the output voltage according to the load impedance. For GFMI topologies to use the aforementioned constant-current clipping protection scheme, it is important to have a good estimation of the impedance of the load being supplied. Thus, the estimated impedance $|Z_{est}|$ is used twofold: i) to trigger the protection scheme once it falls below $|Z_{crit}|$; and ii) to drive the output voltage while in the protection zone by just following Ohm's law, $V_O = |Z_{est}| \cdot I_{max}$.

For DC/DC converters, the impedance calculation can be easily implemented by taking the ratio of the corresponding voltage and current values. However, for time-varying signals, the raw sensed values cannot be used due to the zero crossing nature of the current that will drive the ratio of V/I to undetermined values. The estimation of this V/I ratio for AC signals is discussed in the next section.

B. Impedance Estimation Techniques

Most modern digital protective relays use oversampling and the Discrete Fourier Transform (DFT) to obtain the fundamental phasor values of current and voltage, which subsequently are used to calculate the corresponding fundamental phasor impedance [27]-[28]. In the case of GFMIs, the power calculations rely on transforming the measured raw signals of voltage and current into either: the stationary $\alpha\beta$ reference frame, or the synchronous dq reference frame [13]. Then, the aforementioned transformed values can be used not only to calculate the corresponding active and reactive powers, but also to calculate the peak, and subsequently, the effective RMS values used to estimate the V/I ratio. This peak estimation technique relies on the fact that the post-fault signals attain a sinusoidal or at least a periodic shape, where a 60 Hz fundamental component can be filtered.

In the particular case of the CERTS control scheme, the power measurements are calculated using the stationary $\alpha\beta$ frame, on which the sensed current and voltage signals are decomposed into their corresponding in-quadrature components [13], as shown in equation (1).

$$\begin{bmatrix} x_\alpha \\ x_\beta \end{bmatrix} = \sqrt{2/3} \begin{bmatrix} 1 & -1/2 & -1/2 \\ 0 & \sqrt{3}/2 & -\sqrt{3}/2 \end{bmatrix} \begin{bmatrix} x_a \\ x_b \\ x_c \end{bmatrix} \quad (1)$$

A graphical representation of equation (1) is depicted in Fig. 2, where it is assumed that the instantaneous phase values of voltages and currents can be unfolded on the corresponding set of colored axes separated 120° from each other. The matrix coefficients in equation (1) describe the projections of such instantaneous values onto the in-quadrature $\alpha\beta$ axes. Notice how the -1/2 coefficients project the instantaneous values of phases *b* and *c* onto the α axis, whereas the $\pm\sqrt{3}/2$ coefficients project them onto the β axis.

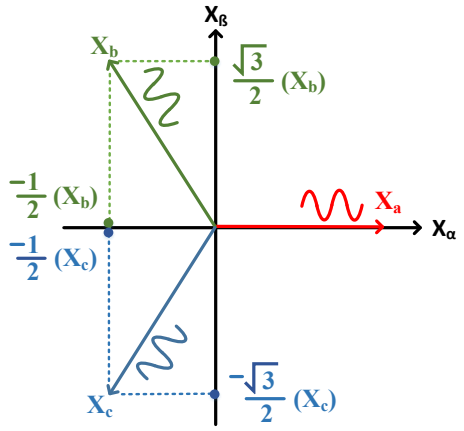

Fig. 2. Graphical Representation of the *abc* to $\alpha\beta$ Transformation.

If the instantaneous sinusoidal three-phase signals are balanced in magnitude and phase, their projections onto the $\alpha\beta$ frame will vary in such a way that, if both $\alpha\beta$ components are added as vectors, their locus describes a circle, as depicted in Fig. 3, whose radius corresponds to the amplitude of the three-phase signals and the frequency of rotation of the main vector corresponds to the fundamental frequency of such signals (ω_c = 377 rad/s). The rotating vector in Fig. 3 resembles the rotating magnetic field induced in the stator of a synchronous machine when a set of balanced three-phase voltages are applied at the stator terminals.

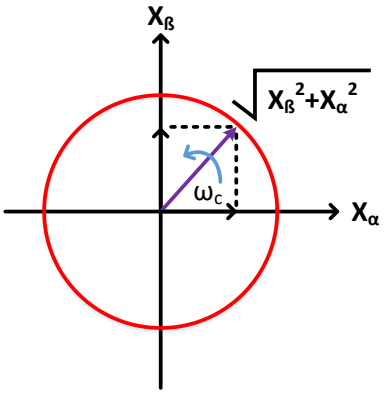

Fig. 3. Circular Locus Described in the $\alpha\beta$-Frame by a Set of Balanced Three-Phase Signals.

The details of the algebraic analysis based upon the space-phasor representation that shows the evolution of equation (1) into the circular locus shown in Fig. 3 can be found in [29]. Using Fig. 3 as a reference, and assuming the use of the $\alpha\beta$ frame, the peak values of voltages and currents can be obtained using equations (2) and (3).

$$I_0^2 = I_{0\alpha}^2 + I_{0\beta}^2 \quad (2)$$

$$V_0^2 = V_{0\alpha}^2 + V_{0\beta}^2 \quad (3)$$

These values are used to calculate the load impedance, given by equation (4).

$$Z_O = \sqrt{\frac{V_0^2}{I_0^2}} \quad (4)$$

Equations (2) through (4) demonstrate that the internal measurements of an inverter can provide very insightful information about the dynamics under fault scenarios in a very similar way CTs and PTs provide signal information to protective relays.

Notice that the above analysis and impedance calculation was based upon sets of balanced three-phase voltages and currents. For the particular case of single-phase GFMIs a different approach must be taken to transform the measured voltages and currents into the $\alpha\beta$ frame. The instantaneous values of the single-phase signals are projected into the α axis. To describe a circular locus with only one sinusoidal signal available, a fictitious β axis is created by projecting a 90° lagging version of the original signal onto such fictitious axis, as shown in Fig. 4. The delay element can be implemented in different ways, but the two most common are: a transpose delay, and a regular derivative. Both implementations can have a significant impact on the initial current overshoot right after fault inception.

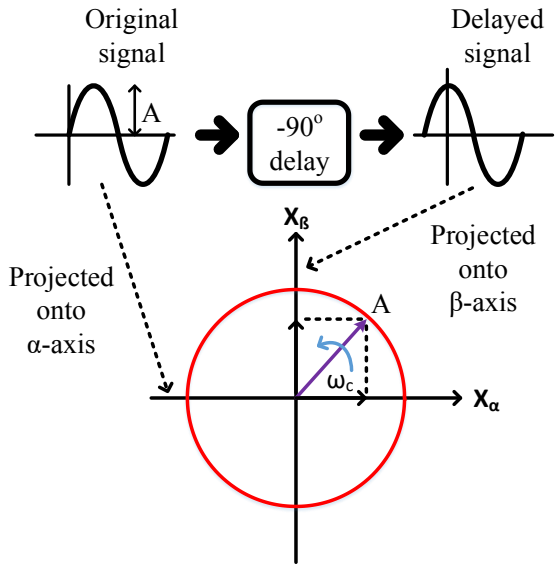

Fig. 4. Projections of a Single-Phase Sinusoidal Signal into the $\alpha\beta$-Frame.

C. *Modified Single-Phase CERTS Model*

The CERTS control scheme was modified to implement the aforementioned current protection scheme as shown in Fig. 5. The $\alpha\beta$ components of the current and voltage are the inputs to the constant-current curtailment protection block, which in return provides the control (triggering) signal and the saturation voltage limits to the dynamic-saturation block that follows the modulated signals from the voltage and frequency-droop control blocks. The phase delay depicted in Fig. 4 was implemented in two ways: i) using a transport delay block, and ii) using a regular derivative block.

III. Experimental Results Comparisons

In order to compare the dynamics under fault scenarios of the model depicted in Fig. 5, experimental tests were performed on a commercially available single-phase inverter, hereinafter referred to as the device under test 1 (DUT 1). DUT 1 is a 5 kW rated GFMI operating at a voltage level of 240 V. Its voltage and current traces under a ground fault [24] with an impedance of Z_f = 2.4 Ω, is compared in Fig. 6 against the traces generated with the modified CERTS model. The traces labeled as Model 1 represent the phase delay implementation using a derivative block, whereas the traces labeled as Model 2 represent the phase delay implementation using a transport delay block. In order to visualize the details in the nuances between the inverter and the simulation model, the magnified portions of the traces focusing on the transient dynamics right after fault inception are shown in Fig. 7. Notice some slight transient mismatches right after fault inception that can be attributed to different output filter characteristics. It is important to clarify that this fraction of the fault current component in particular is complicated to replicate due to manufacturer's reluctance to share information about the filter topology, components, and their respective values. However, the current spike shown by the Model 1 trace is very similar to the experimental current trace followed by a good correlation between the dynamics of two traces in the steady-state period of the fault. The current spike from the trace of Model 2 differs from the experimental current overshoot for about 2 p.u., which can be attributed to the nonlinear dynamics imposed by the transport delay block of the simulation model.

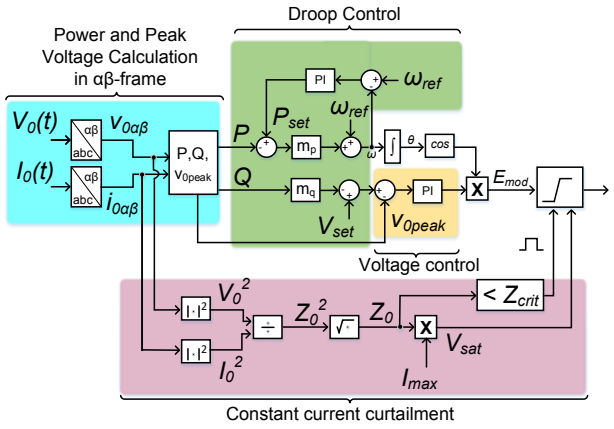

Fig. 5. Modified Single-Phase CERTS Control Scheme with Constant-Current Curtailment Protection.

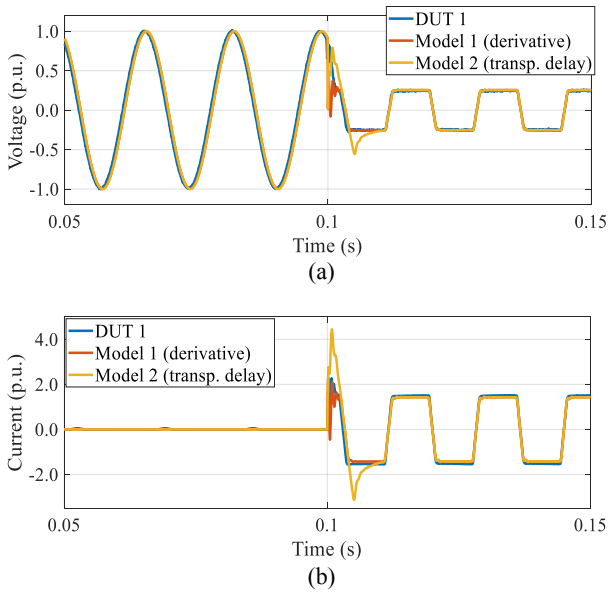

Fig. 6. Fault Dynamics of DUT 1 with the Modified CERTS Models with Different Implementations of the 90º Delay Block. (a) Voltage Response Waveform. (b) Current Response Waveform.

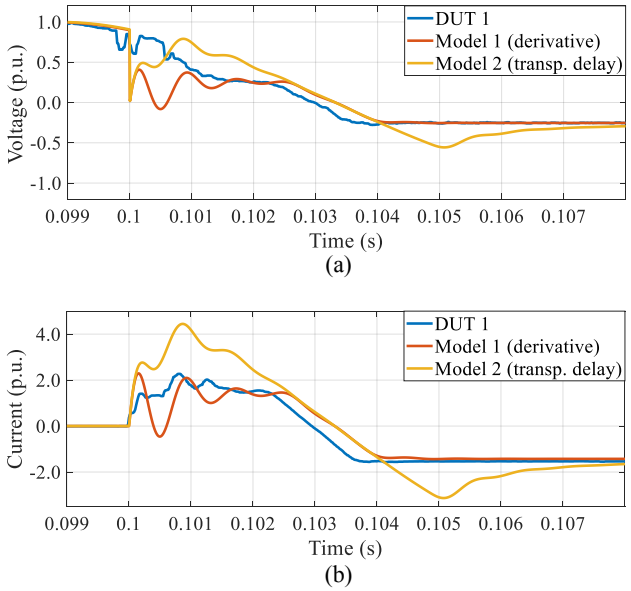

Fig. 7. Magnified Portion of Voltages and Currents Right After the Fault Inception. (a) Voltage Response Waveform. (b) Current Response Waveform.

The second inverter tested, hereinafter referred to as the device under test 2 (DUT 2), is a three-phase GFMI rated 9 kW at 208 V. According to the manufacturer's specifications, the three-phase system is formed with three semi-independent, single-phase GFMI units where the one corresponding to phase-A dictates and communicates the frequency reference to the other two phases. The semi-independence nature of the inverter relies on the fact that each phase regulates its corresponding voltage magnitude without assisting the other phases. On the DC side, only one battery supplies the three single-phase inverters. The operational diagram of such an inverter is depicted in Fig. 8

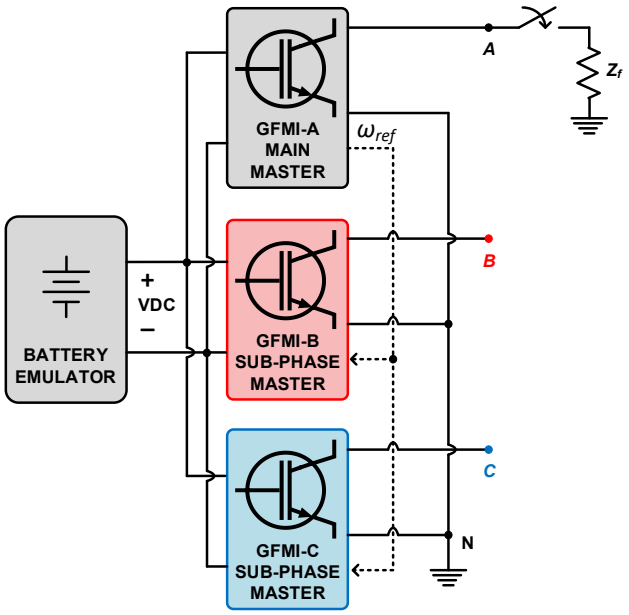

Fig. 8. Operational Diagram of DUT 2 and Single Line to Ground Fault Experimental Setup.

The simulation model for comparison against experimental results was developed using the above operational description. Three single-phase CERTS models with their corresponding current curtailment scheme were used. Also, only the derivative block was used to implement the corresponding 90º phase lag on each single-phase model.

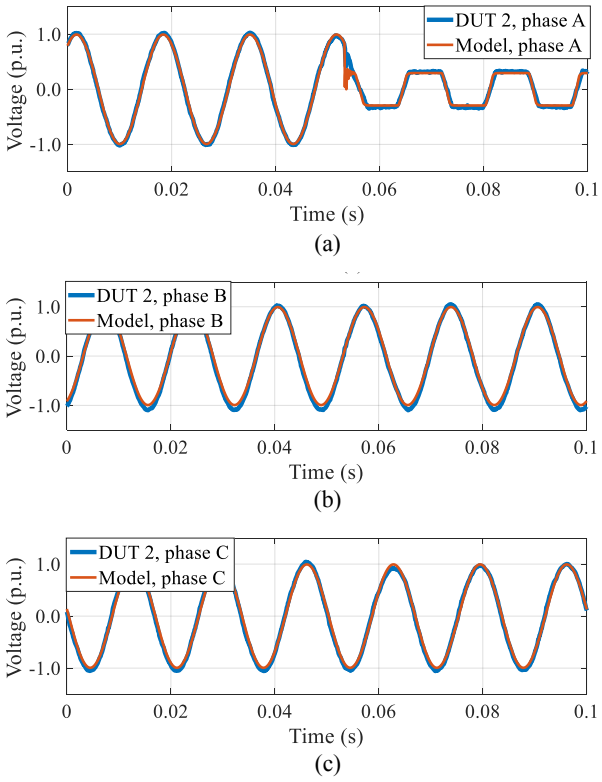

Fig. 9. Comparison of Voltage Waveform Dynamics of the DUT 2 with the Simulation Model. (a) Phase A. (b) Phase B. (c) Phase C.

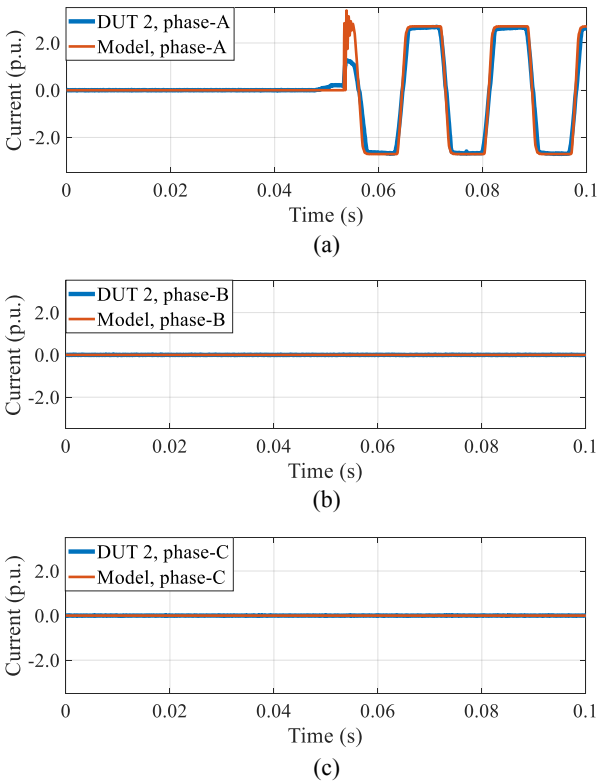

Fig. 10. Comparison of Current Dynamics of DUT 2 with the Simulation Model. (a) Phase A. (b) Phase B. (c) Phase C.

In order to test the aforementioned phase semi-independence under the presence of a ground fault, a single line to ground fault (SLG) was applied to phase-A of DUT 2, with a fault impedance of, $Z_f = 1.5\ \Omega$. The experimental setup is depicted in Fig. 8. The comparison between voltage dynamics right after fault inception is shown in Fig. 9. Notice from these results that due to the independent voltage regulation of each phase, only the faulted phase activates its corresponding curtailment scheme and modulates the voltage according to the calculated impedance from equation (4).

The comparison between current dynamics is shown in Fig. 10. Due to the nature of the experimental test, as illustrated in Fig. 8, phases B and A do not contribute to the fault current, leaving the total fault current contribution to the phase A inverter. From the faulted phase traces shown in Fig. 9 and Fig. 10, it can be observed that after slight transient mismatches due to the output filter, there is a significant correlation between both voltage and current traces of DUT 2 and the proposed model, which demonstrates a high level of accuracy of the proposed simulation model.

Lastly, a double line to ground (DLG) fault was applied to phases A and B of DUT 2. The fault dynamics comparisons for voltage and current of the three phases are shown in Fig. 11 and Fig. 12, respectively. Notice again that after the fault inception transients, the correlation between the fault traces of the simulation model and DUT 2 showed a high degree of accuracy. As with the previous fault case, the phase on which the fault was

not applied (phase C) remained operating regularly due to the semi-independence nature of the inverter.

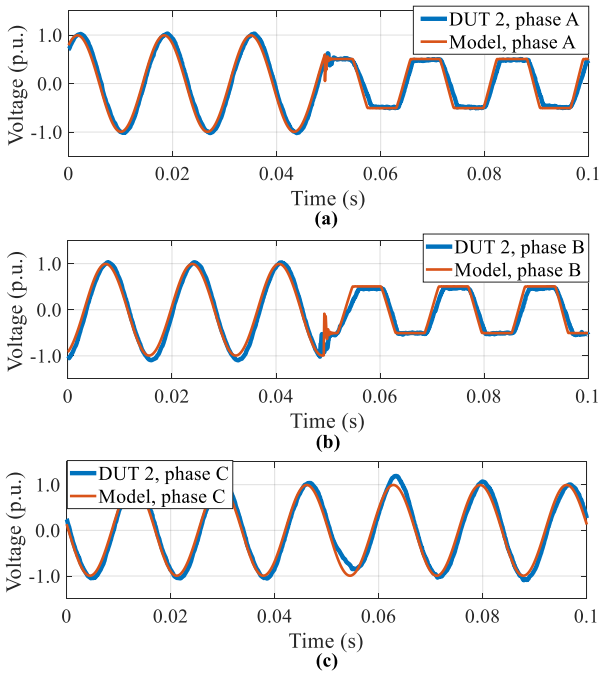

Fig. 11. Comparison of Voltage Waveform Dynamics of the DUT 2 with the Simulation Model for a DLG. (a) Phase A. (b) Phase B. (c) Phase C.

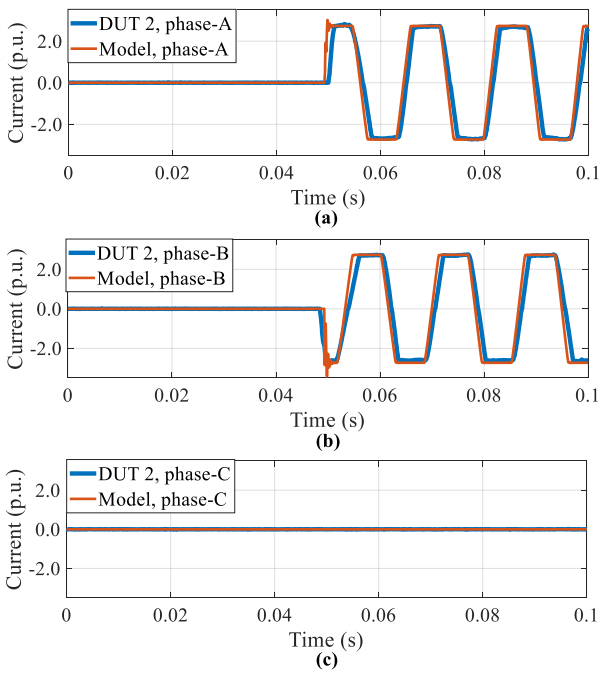

Fig. 12. Comparison of Current Waveform Dynamics of the DUT 2 with the Simulation Model for a DLG. (a) Phase A. (b) Phase B. (c) Phase C.

IV. Conclusions

Most GFMI models focus on steady-state, power sharing, and mode transitions, but additional research and validation is needed for GMFI models during transients or faults when they reach their current limiting controls. This paper proposed and implemented a modified GFMI CERTS model that accurately models the current dynamics during faults. The modifications are based upon the constant current curtailment protection widely used in DC/DC converters, and make use of the original model measurements in the αβ-frame domain. The simulation models were directly compared to hardware experiments of commercially available single-phase and three-phase GFMIs during ground faults. Simulation and experimental results showed very similar transient dynamics.

Acknowledgment

Sandia National Laboratories is a multi-mission laboratory managed and operated by National Technology and Engineering Solutions of Sandia, LLC. a wholly owned subsidiary of Honeywell International, Inc., for the U.S Department of Energy's National Nuclear Security Administration under contract DE-NA-0003525.

References

[1] S. Peake, *Renewable Energy: Power for a Sustainable Future*, 4 Edition. OXFORD.

[2] N. Abi-Samra, *Power Grid Resiliency for Adverse Conditions*. San Diego: Artech House, 2017.

[3] B. J. Walker, "Developing a Resilience Model for North America's Energy Sector Infrastructure," Washington, DC, 2019. [Online]. Available: https://www.energy.gov/oe/articles/developing-resilience-model-north-america-s-energy-sector-infrastructure.

[4] M. J. Reno, S. Brahma, A. Bidram, and M. E. Ropp, "Influence of Inverter-Based Resources on Microgrid Protection: Part 1: Microgrids in Radial Distribution Systems," *IEEE Power and Energy Magazine*, 2021.

[5] R. H. Lasseter and P. Piagi, "Microgrid: A Conceptual Solution," 2004.

[6] B. Kroposki *et al.*, "Achieving a 100% Renewable Grid: Operating Electric Power Systems with Extremely High Levels of Variable Renewable Energy," *IEEE Power Energy Mag.*, vol. 15, no. 2, pp. 61–73, 2017, doi: 10.1109/MPE.2016.2637122.

[7] A. Bidram, V. Nasirian, A. Davoudi, and F. L. Lewis, *Cooperative Synchronization in Distributed Microgrid Control.*, 1st editio. Springer, 2017.

[8] Q.-C. Zhong and T. Hornik, *Control of Power Inverters in Renewable Energy and Smart Grid Integration*. John Wiley & Sons, 2013.

[9] Q.-C. Zhong, *Power Electronics-Enabled Autonomous Power Systems Next Generation Smart Grids*. Chicago: Wiley IEEE Press, 2020.

[10] J. Johnson, R. Ablinger, R. Bruendlinger, B. Fox, and J. Flicker, "Interconnection Standard Grid-Support Function Evaluations Using an Automated Hardware-in-the-Loop Testbed," *IEEE J. Photovoltaics*, vol. 8, no. 2, pp. 565–571, Mar. 2018, doi: 10.1109/JPHOTOV.2018.2794884.

[11] J. Hernandez-Alvidrez, N. S. Gurule, M. J. Reno, J. D. Flicker, A. Summers, and A. Ellis, "Method to Interface Grid-Forming Inverters into Power Hardware in the Loop Setups," 2020.

[12] J. Johnson *et al.*, "Distribution voltage regulation using extremum seeking control with power hardware-in-the-loop," *IEEE J. Photovoltaics*, vol. 8, no. 6, pp. 1824–1832, Nov. 2018, doi: 10.1109/JPHOTOV.2018.2869758.

[13] R. Teodorescu, M. Liserre, and P. Rodríguez, *Grid Converters for Photovoltaic and Wind Power Systems*, First. Wiley, 2011.

[14] P. Kundur, *Power System Stability and Control*. Tata McGraw-Hill, 1993.

[15] J. Flicker, J. Hernandez-Alvidrez, M. Shirazi, J. Vandermeer, and W. Thomson, “Grid Forming Inverters for Spinning Reserve in Hybrid Diesel Microgrids,” Dec. 2020, pp. 1–5, doi: 10.1109/pesgm41954.2020.9281497.

[16] W. Du, K. P. Schneider, F. K. Tuffner, Z. Chen, and R. H. Lasseter, “Modeling of Grid-Forming Inverters for Transient Stability Simulations of an all Inverter-based Distribution System,” pp. 1–5, 2019, doi: 10.1109/isgt.2019.8791620.

[17] W. Du, R. H. Lasseter, and A. S. Khalsa, “Survivability of autonomous microgrid during overload events,” *IEEE Trans. Smart Grid*, vol. 10, no. 4, pp. 3515–3524, Jul. 2019, doi: 10.1109/TSG.2018.2829438.

[18] H. Bevrani, B. François, and T. Ise, *Microgrid Dynamics and Control*. New Jersey: Wiley & Sons, 2017.

[19] ABB;, *PCS100 ESS Grid Connect Interface for Energy Storage Systems User Manual*, 1st Editio. .

[20] B. B. Johnson, M. Sinha, N. G. Ainsworth, F. Dorfler, and S. V. Dhople, “Synthesizing Virtual Oscillators to Control Islanded Inverters,” *IEEE Trans. Power Electron.*, vol. 31, no. 8, pp. 6002–6015, Aug. 2016, doi: 10.1109/TPEL.2015.2497217.

[21] J. Brian, L. Yashen, E. Joe, L. Robert, E. Abraham, and D. Kirshen, “Grid-forming Inverters for Low-inertia Power Systems,” *Workshop on Low-inertia Grids. Univertsity of Washington.*, 2019. https://lowinertiagrids.ece.uw.edu/ (accessed Nov. 02, 2019).

[22] J. Hernandez-Alvidrez, A. Summers, M. J. Reno, J. Flicker, and N. Pragallapati, “Simulation of Grid-Forming Inverters Dynamic Models using a Power Hardware in the Loop Testbed.,” in *46th IEEE Photovoltaic Specialists Conference*, 2019, no. July.

[23] R. Darbali-Zamora, N. S. Gurule, J. Hernandez-Alvidrez, S. Ginzalez, and M. J. Reno, “Performance of a Grid-Forming Inverter Under Balanced and Unbalanced Voltage Phase Angle Jump Conditions,” 2021.

[24] N. S. Gurule, J. Hernandez-Alvidrez, M. J. Reno, A. Summers, S. Gonzalez, and J. Flicker, “Grid-forming Inverter Experimental Testing of Fault Current Contributions,” in *Conference Record of the IEEE Photovoltaic Specialists Conference*, Jun. 2019, pp. 3150–3155, doi: 10.1109/PVSC40753.2019.8980892.

[25] N. S. Gurule, J. Hernandez-Alvidrez, R. Darbali-Zamora, M. J. Reno, and J. D. Flicker, “Experimental Evaluation of Grid-Forming Inverters under Unbalanced and Fault Conditions,” in *IECON Proceedings (Industrial Electronics Conference)*, Oct. 2020, vol. 2020-October, pp. 4057–4062, doi: 10.1109/IECON43393.2020.9254562.

[26] N. Mohan, T. M. Undeland, and W. P. Robbins, *POWER ELECTRONICS. Converters, Applications, and Design.*, 3 Edition. Wiley.

[27] S. M. Brahma, P. L. De Leon, and R. G. Kavasseri, “Investigating the option of removing the antialiasing filter From digital relays,” *IEEE Trans. Power Deliv.*, vol. 24, no. 4, pp. 1864–1868, 2009, doi: 10.1109/TPWRD.2009.2028802.

[28] A. T. Johns and S. K. Salman, *Digital Protection for Power Systems (I E E POWER ENGINEERING SERIES)*, 1 Edition. .

[29] A. Yazdani and R. Iravani, *Voltage-sourced converters in power systems : modeling, control, and applications*. IEEE Press/John Wiley, 2010.